

# Optical and structural properties of $\text{Zn}_{1-x}\text{Mg}_x\text{O}$ ceramic materials

Zayani Jaafar Othman · Adel Matoussi ·  
Filippo Fabbri · Francesca Rossi · Giancarlo Salviati

Received: 27 November 2013 / Accepted: 21 January 2014 / Published online: 4 February 2014  
© Springer-Verlag Berlin Heidelberg 2014

**Abstract** This paper reports structural, optical and cathodoluminescence characterizations of sintered  $\text{Zn}_{1-x}\text{Mg}_x\text{O}$  composite materials. The effects of MgO composition on these film properties have been analyzed. X-ray diffraction (XRD) confirms that all composites are polycrystalline with prominent hexagonal wurtzite structure along two preferred orientations (002) and (101) for the crystallite growth. Above doping content  $x = 10\%$ , the formation of the hexagonal ZnMgO alloy phase and the segregation of the cubic MgO phase start. From reflectance and absorption measurements, we determined the band gap energy which tends to increase from 3.287 to 3.827 eV as the doping content increases. This widening of the optical band gap is explained by the Burstein–Moss effect which causes a significant increase of electron concentration ( $2.89 \times 10^{18}$ – $5.19 \times 10^{20} \text{ cm}^{-3}$ ). The luminescent properties of the  $\text{Zn}_{1-x}\text{Mg}_x\text{O}$  pellets are studied by cathodoluminescence (CL) at room and liquid nitrogen temperatures under different electron beam excitations. At room temperature, the CL spectra of the  $\text{Zn}_{1-x}\text{Mg}_x\text{O}$  composites exhibit a dominant broad yellow-green light band at 2.38 eV and two ultraviolet emission peaks at 3.24 and 3.45 eV corresponding to the luminescence of the hexagonal ZnO and ZnMgO structures, respectively. For the doped ZnO samples, it reveals also new red peaks at 1.72 and 1.77 eV assigned to impurities' emissions. However, the CL spectra recorded at 77 K show the presence of excitonic emission peaks related to recombination of free exciton ( $X_A$ ),

neutral donor-bound excitons ( $D^0X$ ) and their phonon replicas. The CL intensity and energy position of the green, red and ultraviolet emission peaks are found to depend strongly on the MgO doping content. The CL intensity of the UV and red emissions is more enhanced than the green light when the MgO content increases. CL imaging analysis shows that the repartition of the emitting centers in  $\text{Zn}_{1-x}\text{Mg}_x\text{O}$  composites is intimately connected to the film composition and surface morphology.

## 1 Introduction

During the last few years, zinc oxide (ZnO) has gained much interest in research activity and industrial applications ranging from transparent electrodes (TCO) in solar cells [1, 2], gas sensors [3, 4], spintronic devices [5, 6], light-emitting diodes (LEDs) [7, 8] to surface acoustic wave devices [9], based specially on its wide direct band gap (3.35 eV) and large exciton binding energy (60 meV) at room temperature [10]. To extend its optoelectronic application in the infrared and ultraviolet wavelength regions, many researchers have attempted to introduce proper ions such as Cd, Co and Mg into the ZnO lattice to adjust the energy band structure [11–15]. Acharya et al. [11] reported the growth of wurtzite  $\text{Zn}_{1-x}\text{Cd}_x\text{O}$  ( $x \leq 0.25$ ) on glass substrates by the spray pyrolysis technique. They found that the optical band gap could be tuned from that of ZnO (3.25 eV) to 2.94 eV at Cd doping content  $x = 25\%$ . Therefore, ZnMgO thin films have been prepared by many techniques such as spray pyrolysis, pulsed laser deposition, molecular beam epitaxy (MBE), metalorganic vapor-phase epitaxy (MOVPE) and sol–gel process [16]. Reports have demonstrated that the ternary alloys  $\text{Zn}_{1-x}\text{Mg}_x\text{O}$  with a wide range of Mg composition  $x$  from 0 to 49% still

Z. J. Othman (✉) · A. Matoussi  
Laboratory of Composite Ceramic and Polymer Materials,  
Scientific Faculty of Sfax, Sfax, Tunisia  
e-mail: jaafar.zayani@yahoo.fr

F. Fabbri · F. Rossi · G. Salviati  
Institute of Materials for Electronics and Magnetism (IMEM)  
CNR, Parma University, Parma, Italy

maintained their hexagonal lattice structure due to the similar ionic radius of  $\text{Mg}^{2+}$  (0.57 Å) and  $\text{Zn}^{2+}$  (0.60 Å), and the corresponding energy band gap could be increased from 3.34 to 4.19 eV [17, 18]. Ohtomo et al. [13] have reported the first synthesis of high-quality, single-phase  $\text{Mg}_x\text{Zn}_{1-x}\text{O}$  thin films with Mg concentrations up to 33 % at due to the non-equilibrium nature of pulsed laser deposition (PLD) growth. Chunming Jin [18] has evidenced the epitaxial growth of hexagonal  $\text{MgZnO}$  films on sapphire (0001) substrates with single-crystalline quality where the band gap of these films can be controlled from 3.36 to 4.12 eV by changing the Mg content. The effect of increasing Mg content in the ZnO films was found to reduce the defect emission and to improve strongly the bright excitonic photoluminescence at room temperature. Many recent papers [16–23] have demonstrated that the optical and luminescent properties of  $\text{ZnMgO}$  films are very sensitive to the defect density, chemical stoichiometry and crystalline microstructure that depend strongly on the growth temperature and the Mg doping concentration. Single-phase and polycrystalline  $\text{Zn}_{1-x}\text{Mg}_x\text{O}$  pellets were synthesized using solid-reaction method which had extremely high green and orange with increase of MgO alloying [22]. Recently, Lui et al. [23] have observed S-shaped temperature dependence of the near-band PL emissions and Stokes red shifts of about 365 meV in high-Mg-content single-phase wurtzite  $\text{Mg}_x\text{Zn}_{1-x}\text{O}$  ( $0.27 < x < 0.55$ ) epilayers. They explained these behaviors in terms of localized exciton emissions caused by the Mg compositional fluctuations. In this paper, we study the effect of MgO doping contents on structural, optical and luminescent properties of  $\text{Zn}_{1-x}\text{Mg}_x\text{O}$  composites prepared by the solid-state reaction technique.

## 2 Experimental details

The  $\text{Zn}_{1-x}\text{Mg}_x\text{O}$  composites were prepared by using a conventional solid-state sintering method. Different weight contents of MgO ( $x = 0\text{--}40\%$ ) were added to ZnO powder (purity  $\sim 99.99\%$ ) which was homogeneously milled in an agate mortar and then calcined in air at 500 °C for 3 h. The  $\text{Zn}_{1-x}\text{Mg}_x\text{O}$  powders were pressed into pellets (of 1 mm thickness and 6 mm diameter) and sintered at a high temperature of 1200 °C for 24 h with a heating rate of 10 °C/min. The pellets were then cooled slowly to room temperature. X-ray diffraction (XRD) with  $\text{Cu-K}\alpha$  radiation wavelength of 0.15406 nm was used to determine the crystal structure of the  $\text{ZnMgO}$  samples in the scan range  $2\theta = 20^\circ\text{--}60^\circ$ . The optical properties of the  $\text{ZnMgO}$  pellets were examined in the wavelength range 200–1800 nm by using the UV–VIS–NIR spectrophotometer

(SHIMADZU UV-3101PC). The luminescent properties were studied by cathodoluminescence (CL) spectroscopy and monochromatic imaging under electron beam energy and beam current  $I = 5$  nA. The CL spectra were recorded at room and liquid nitrogen temperature by using a Gatan MonoCL2 system installed on a Cambridge S-360 SEM coupled with a multialkali photomultiplier detector [24].

## 3 Results and discussions

### 3.1 Structural properties

Figure 1 shows the XRD patterns of doped ZnO samples with different MgO contents. For undoped ZnO sample, we noticed the appearance of five prominent diffraction peaks at  $2\theta = 31.81^\circ, 34.47^\circ, 36.31^\circ, 46.60^\circ$  and  $56.63^\circ$ , which can attributed to the (100), (002), (101), (102) and (110) planes of hexagonal wurtzite ZnO (JCPDS card 36-1451). It reveals that the MgO doping does not affect the hexagonal structure of all doped ZnO samples, but secondary phases can be formed at higher concentration. Also, the degree of texture is strongly influenced by the level of MgO doping concentration. One can observe that all the composites have (002) and (101) as the preferred orientations for the crystallite growth with texture coefficient about 47 and 26 %, respectively [25, 26]. With doping content up to  $x = 20\%$ , two distinct diffraction peaks appear at  $36.7^\circ$  and  $42.3^\circ$  corresponding, respectively, to (111) and (200) planes of cubic MgO phase (JCPDS card No. 78-0430). The intensity of the rock-salt cubic peaks is found to increase significantly compared to hexagonal ones which contribute quantitatively about 15 % of textured grains. This result indicates a strong segregation of the MgO phase in the ZnO wurtzite structure. The limit solubility of MgO in the ZnO host lattice is found to be 10 % which agrees well with the result of Kumar et al. [27] in  $\text{Zn}_{1-x}\text{Mg}_x\text{O}$  ( $x \leq 20\%$ ) systems synthesized by sol–gel method.

In Fig 1b, one can see clearly the presence of small peak at  $34.68^\circ$  which can be identified to the (002) reflection plane of the  $\text{ZnMgO}$  hexagonal structure [28–30]. Zheng et al. [30] showed single-crystalline wurtzite structure of  $\text{Zn}_{0.51}\text{Mg}_{0.49}\text{O}$  films where the (002) diffraction peak appeared close to the angles  $2\theta = 34.7^\circ$ . Furthermore, it has been reported that up to 15 mol % addition of MgO, the formation of alloy  $\text{ZnMgO}$  phase takes place [31]. Recently, Singh et al. [32] have obtained by the sol–gel method single-wurtzite  $\text{Zn}_{1-x}\text{Mg}_x\text{O}$  thin films for Mg content  $x \leq 25\%$ ; above this concentration, phase segregations are initiated and a mixed phase of hexagonal and cubic crystal structure is observed.

**Fig. 1** **a** XRD patterns of Zn<sub>1-x</sub>Mg<sub>x</sub>O composites, **b** enlarged detail of diffraction spectra

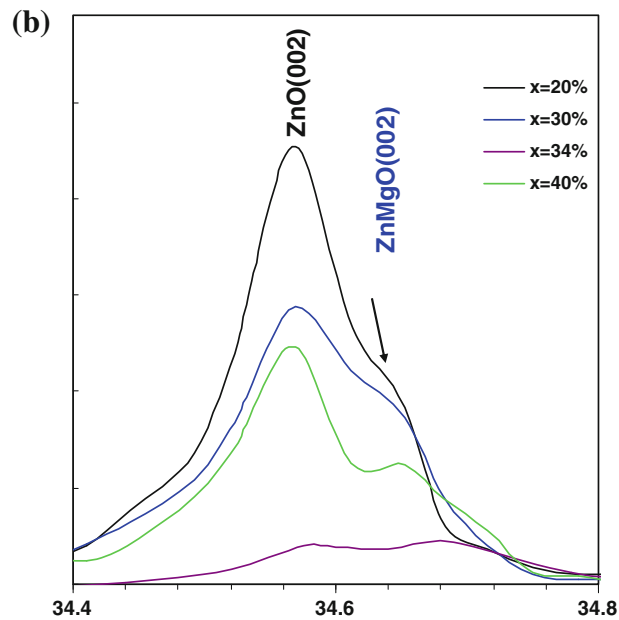
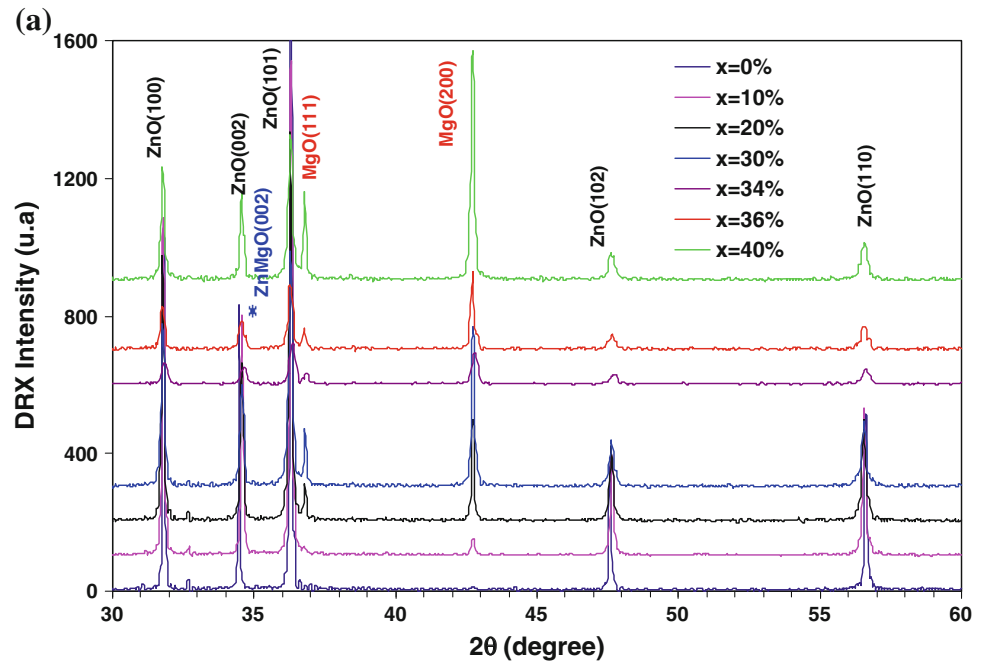


**Table 1** Lattice constants, biaxial strains, stress and the average grain sizes for all the compositions

| MgO (wt%) | $a$ (Å) | $c$ (Å) | $\epsilon_{xx}$ | $\epsilon_{zz}$ | $\sigma_{zz}$ (GPa) | $D$ (nm) |
|-----------|---------|---------|-----------------|-----------------|---------------------|----------|
| 0         | 3.2448  | 5.1984  | -0.00154        | -0.00156        | 0.355               | 109.554  |
| 10        | 3.2475  | 5.1868  | -0.00072        | -0.00379        | 0.860               | 101.511  |
| 20        | 3.24974 | 5.1834  | -0.000048       | -0.00444        | 1.007               | 100.620  |
| 30        | 3.2501  | 5.1828  | 0.000065        | -0.00456        | 1.035               | 89.558   |
| 34        | 3.2506  | 5.18327 | 0.000242        | -0.004479       | 1.016               | 48.465   |
| 36        | 3.2508  | 5.18294 | 0.000304        | -0.004544       | 1.030               | 46.259   |
| 40        | 3.2509  | 5.18151 | 0.000329        | -0.004817       | 1.092               | 42.978   |

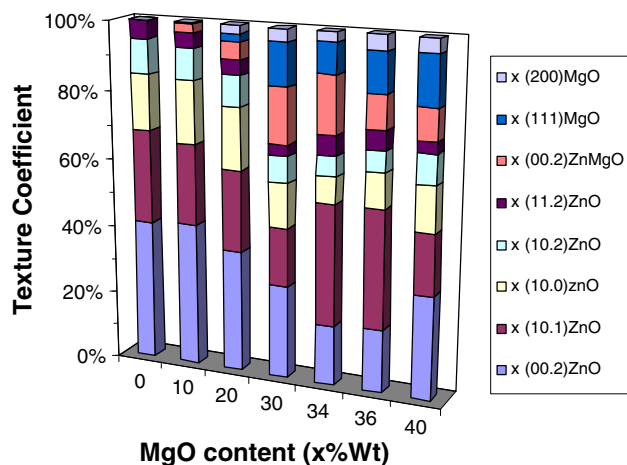


**Fig. 2** Variation of texture coefficient versus MgO doping content for all crystallographic orientations

Furthermore, it shows that the (002) peak is slightly shifted to higher diffraction angles where its width is found to increase from  $0.07^\circ$  to  $0.22^\circ$  with increasing MgO content from  $x = 0$  to 40 %, respectively. This indicates a decrease in the  $c$ -axis lattice parameter which can result from the partial incorporation of  $Mg^{2+}$  ion in the host ZnO matrix at the substitution  $Zn^{2+}$  sites [27, 33]. The lattice constants ( $a$ ,  $c$ ), the average grain sizes ( $D$ ) and the biaxial residual stress ( $\sigma_{zz}$ ) in all ZnMgO samples were calculated and are reported in (Table 1). The variation of texture coefficient versus MgO doping content for all crystallographic orientations is presented in the Fig. 2.

When the doping content is increased ( $x = 0$ –40 %), the average grain size is found to decrease from 109.55 to 42.97 nm. Moreover, one can point out that the crystalline quality deteriorates with the increase of MgO content. In fact, the residual strain ( $\varepsilon_{xx}$ ) is compressive below  $x = 20$  %, and above this concentration it becomes tensile and increases gradually. The biaxial stress ( $\sigma_{zz}$ ) along the  $c$ -axis is increased from 0.35 to 1.03 GPa as the doping concentration is varied from 0 to 40 %.

### 3.2 Optical properties

To investigate the optical properties of the fabricated ZnMgO composites, we have recorded at room temperature the diffuse reflectance ( $R$ ) spectra in the UV–VIS–NIR region (200–2400 nm). Figure 3 presents the reflectance spectra of the ZnMgO samples for different MgO doping contents. One can see that the average reflectance is found to vary from 75 to 93 % in the visible region for all the samples. The same behavior is observed in the UV region in which the reflectance increases about 50 to 70 % as the MgO doping content increases. It shows that below a wavelength of 400 nm, the reflectance spectra tend to shift

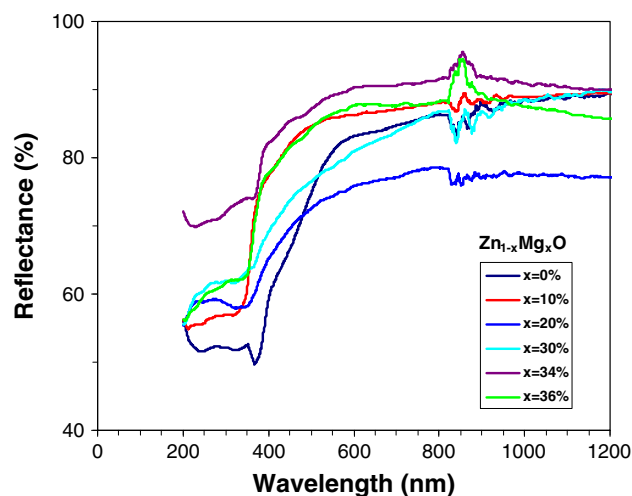


**Fig. 3** Reflectance spectra of  $Zn_{1-x}Mg_xO$  pellets measured at room temperature

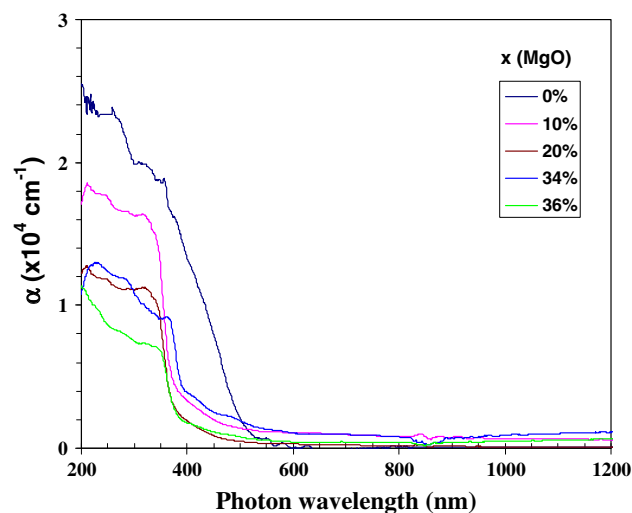


**Fig. 4** Absorption coefficient spectra of  $Zn_{1-x}Mg_xO$  pellets measured at room temperature

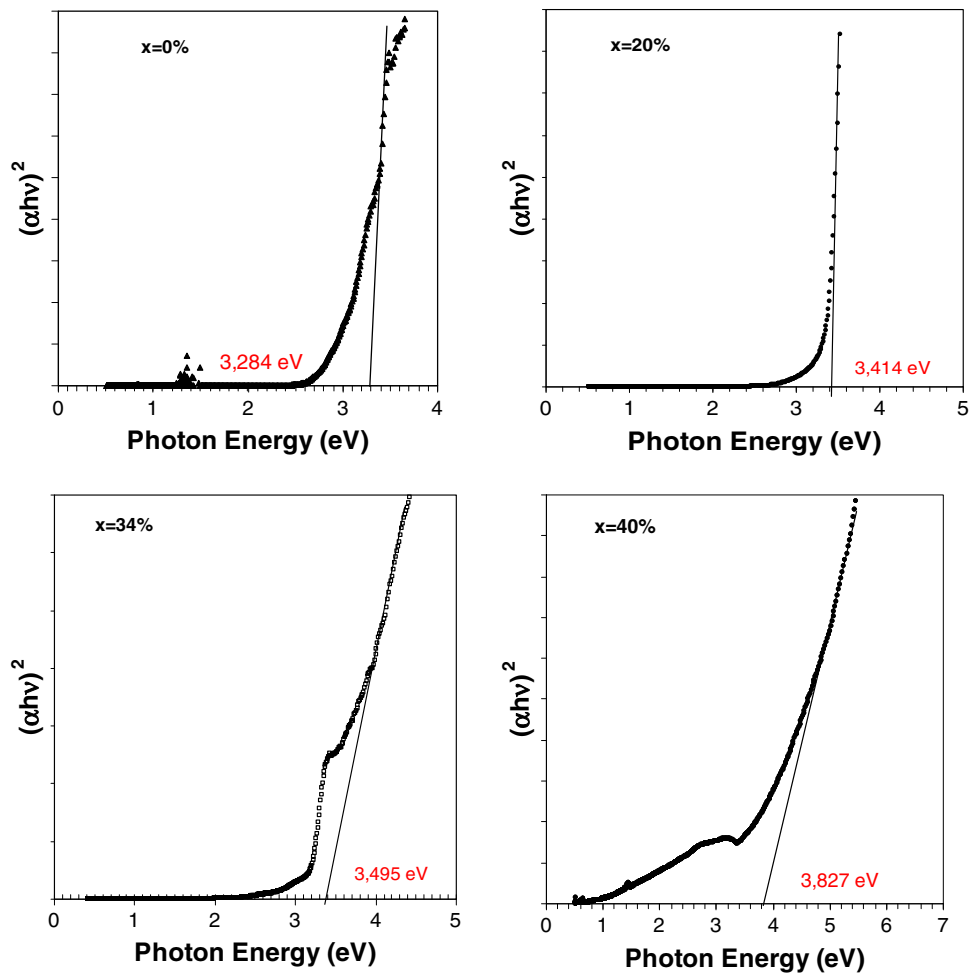
toward shorter wavelengths. This decrease starts from the absorption edges situated near the optical band gap. Here, it must be noticed that all ZnMgO samples have very low transparency in the wavelength range 200–1800 nm. It is well known that for weakly absorbing samples, the Kubelka–Munk function [34, 35] is commonly used to determine the optical absorption coefficient ( $\alpha$ ) from the diffuse reflectance  $R$  which is given by the relation:

$$\alpha = \frac{F(R)}{t} = \frac{(1 - R)^2}{2Rt} \quad (1)$$

where  $t \approx 1.2$  mm is the thickness of  $Zn_{1-x}Mg_xO$  pellets.

Figure 4 shows the absorption coefficient of  $Zn_{1-x}Mg_xO$  pellets measured at room temperature. When the doping concentration is increased, we observe clearly a blue shifting of the absorption spectra toward the UV region,

**Fig. 5** Plots of  $(\alpha hv)^2$  versus photon energy of Zn<sub>1-x</sub>Mg<sub>x</sub>O composites



indicating an increase of the band gap. After that, we used Tauc’s procedure to evaluate precisely the optical band gap from the plots  $(\alpha hv)^2$  versus the photon energy  $hv$ . As shown in Fig. 5a–g, the existence of linear segment on these plots verifies the existence of direct optical transition where its extrapolating to the axis of photon energy [corresponding to  $(\alpha hv)^2 = 0$ ] permits determining the band gap energy  $E_g$  (see Table 2). We see that the values of  $E_g$  increase from 3.28 eV to 3.41, 3.52 and 3.82 at Mg doping content  $x = 0, 20, 36$  and 40 %, respectively. Nidhi Adhlakra et al. [36] have reported similar results for doped ZnO samples with MgO concentrations between 0 and 50 %. However, this increment in the band gap  $E_g$  is believed to be caused by the Burstein–Moss effect [37–39]. Shan et al. [37] have demonstrated that the Mg doping in ZnO leads to an obvious increase in the carrier concentration and a blue shift of the band gap. From the XRD analysis, the texture coefficient of hexagonal ZnMgO phase is very low (<8 %) and its contribution to the increase in  $E_g$  should be neglected. This exclusion is well verified since the band gap broadening is not described by Vegard’s law for solid ternary alloys [38]. As shown in Fig. 6a, the

**Table 2** Variation of the band gap and Urbach tail energies of Zn<sub>1-x</sub>Mg<sub>x</sub>O composites

| MgO content (x %) | $E_g$ (eV)    | $E_U$ (eV) |
|-------------------|---------------|------------|
| 0                 | 3.287 ± 0.013 | 0.768      |
| 10                | 3.365 ± 0.012 | 0.726      |
| 20                | 3.414 ± 0.015 | 0.531      |
| 30                | 3.435 ± 0.102 | 0.633      |
| 34                | 3.495 ± 0.122 | 0.779      |
| 36                | 3.523 ± 0.125 | 0.819      |
| 40                | 3.827 ± 0.123 | 0.886      |

band gap widening  $\Delta E_g$  compared to that of ZnO bulk film ( $E_{g0} = 3.3$  eV) is perfectly described by a linear fit with the carrier concentration ( $n^{2/3}$ ), as given by the relationship of Burstein–Moss effect [39]:

$$\Delta E_g = \frac{h}{8m^*} \left(\frac{3}{\pi}\right)^{2/3} n^{2/3} \tag{2}$$

where  $h$  is the Planck’s constant ( $4.13 \times 10^{-15}$  eV s);  $m^*$  is the electron mass ( $9.11 \times 10^{-31}$  kg) and  $n$  is the electron

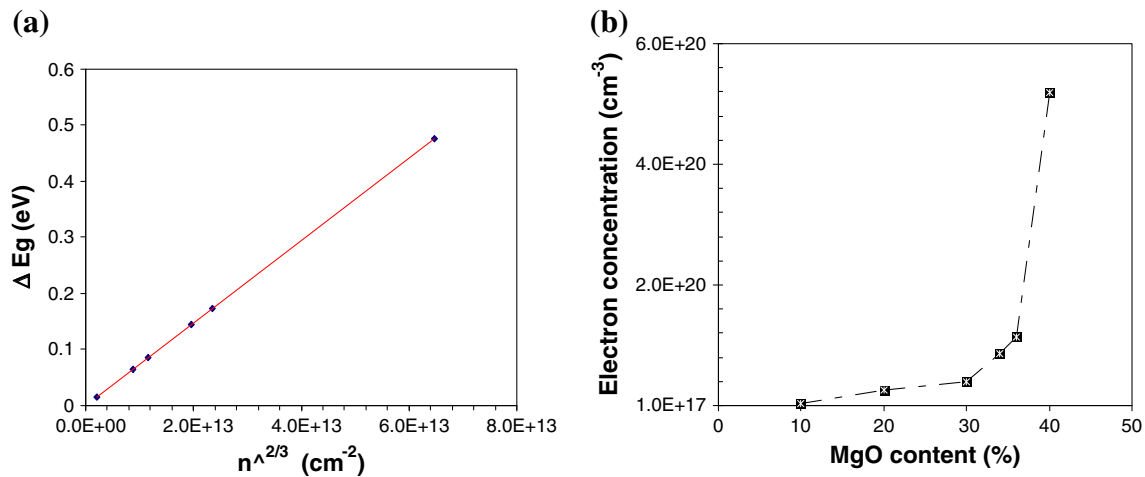


**Fig. 6** **a** Fitted band gap broadening  $\Delta E_g$  with the Burstein–Moss model. **b** Variation free electron concentration with the increase of MgO content

concentration which varies from  $2.89 \times 10^{18}$  to  $5.19 \times 10^{20} \text{ cm}^{-3}$  as the doping content  $x$  is increased from 10 to 40 %, respectively (see Fig. 6b).

We have determined the Urbach tail  $E_U$  of the composites from the linear slope of the curves  $\ln \alpha$  vs the photon energy and use the equation [40]:

$$\alpha = \alpha_0 \exp\left(\frac{h\nu - E_g}{E_U}\right) \quad (3)$$

The  $E_U$  value has been calculated and is presented in Table 2. We see that the Urbach energy decreases from 0.76 to 0.53 eV when the doping level increases from 0 to 20 % and then increases to 0.88 eV for  $x = 40$  %. These values are higher and can be correlated with the increase of structural stress in our prepared  $\text{Zn}_{1-x}\text{Mg}_x\text{O}$  materials.

However, the change in the Urbach tail energy above the doping content  $x = 20$  % may be caused by the MgO segregation phenomenon and also by the increase in free electron concentration which acts as scattering centers. This phenomenon may be due to the compositional inhomogeneity and/or crystalline imperfection in  $\text{ZnMgO}$ , as suggested by Akihiro Wakahara [41] in epitaxial  $\text{Zn}_{1-x}\text{Mg}_x\text{O}$  films grown on sapphire substrates at 500 °C by pulsed laser deposition.

### 3.3 Cathodoluminescence properties

Figure 7a shows the CL spectra of the  $\text{Zn}_{1-x}\text{Mg}_x\text{O}$  composites measured at room temperature under an electron beam energy of 20 keV. The spectrum of ZnO sample is dominated by the near-band edge (NBE) emission at 382 nm (3.24 eV) corresponding to the excitonic recombination. A broadened peak at  $\lambda = 520$  nm (2.38 eV) is observed which corresponds to yellow-green luminescence (YL/GL). The origin of this emission band is attributed to

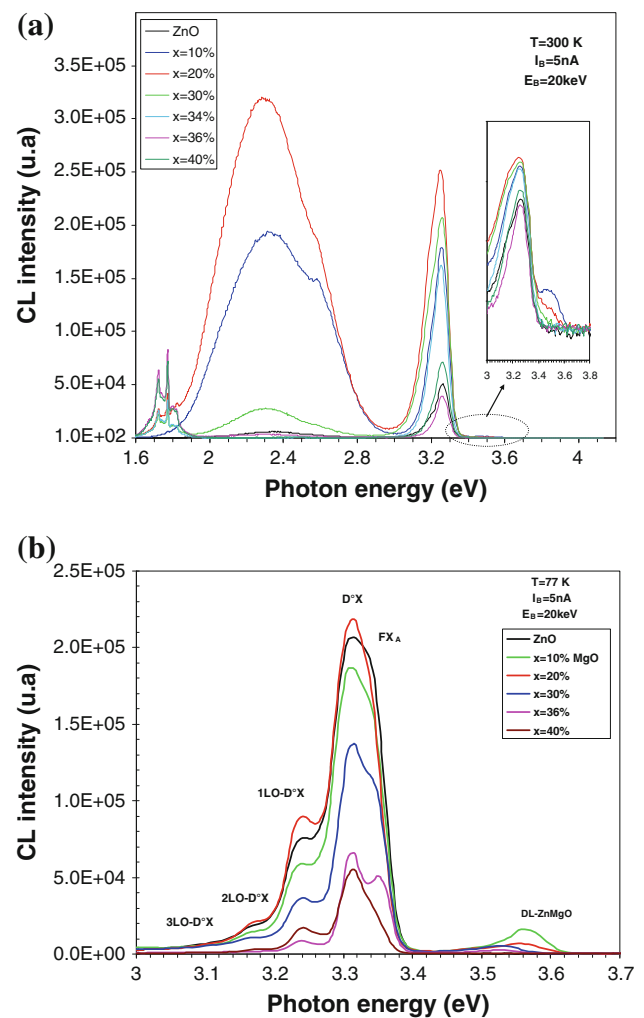


**Fig. 7** **a** Cathodoluminescence spectra of  $\text{Zn}_{1-x}\text{Mg}_x\text{O}$  composites acquired at room temperature, **b** liquid nitrogen temperature 77 K under electron beam energy  $E_B = 20$  keV and beam current excitation  $I_B = 5$  nA

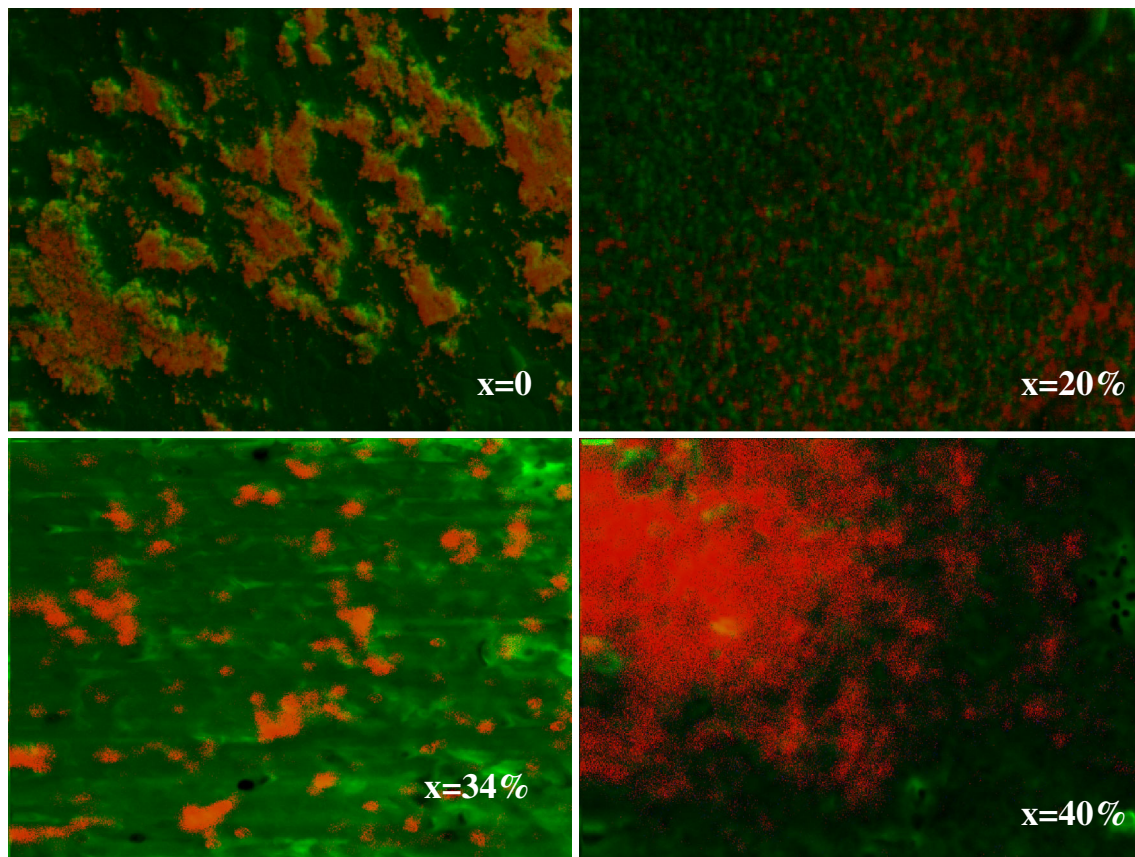


**Fig. 8** CL imaging of Zn<sub>1-x</sub>Mg<sub>x</sub>O composites taken at  $\lambda = 382$  nm

the presence of various intrinsic defects, such as zinc interstitials and oxygen vacancies, where the oxygen vacancies are major defects generating green light in wide band gap ZnO [14, 21, 24, 42–44]. Minami et al. [44] proposed that the yellow-green emission in ZnO might be associated to a transition within a self-activated center formed by a double-ionized zinc vacancy ( $V_{Zn}^{-2}$ ) and a single-ionized interstitial  $Zn_i^+$  at the one and/or two nearest-neighbor interstitial sites. Ogawa et al. [14] have attributed the green emission of ZnO to the recombination of electrons of the singly ionized center ( $V_O^{\cdot}$ ) with the photoexcited holes in the valence band. Therefore, it must be pointed out that the CL spectra of the doped ZnO films are found to depend significantly on the MgO composition. For all Zn<sub>1-x</sub>Mg<sub>x</sub>O samples ( $x \geq 10$  %), the spectra exhibit additional CL red peaks at 1.71 and 1.77 eV, which are assigned to Cr and Fe defect emissions incorporated in the MgO material [45–48]. El Hichou et al. [43] ascribed the red emission (670–700 nm) to oxygen defects in F-doped and Sn-doped ZnO thin films prepared at 450 °C by the spray pyrolysis method. It reveals also a weak UV emission around 3.46 eV for doped ZnO with MgO content equal to  $x = 10, 20$  and  $30$  %. This emission is blue shifted about 120 meV than that of free exciton in ZnO bulk film

(3.35 eV). The CL intensity and energy position of the UV peaks are found to depend strongly on the crystalline quality and on the MgO doping content. It is clearly seen that the addition of MgO in ZnO leads to enhancement of the near-band gap emissions. Figure 7b shows the CL spectra recorded at 77 K with exciting electron beam energy  $E = 20$  keV in the wavelength range 300–450 nm. The spectra display violet peaks at 3.35, 3.31, 3.23 and 3.17 eV that are attributed to ZnO hexagonal structure. These peaks are identified as free exciton emission ( $FX_A$ ) and neutral donor-bound exciton ( $D^0X$ ) and its phonon replicas (denoted by  $D^0X-1LO$  and  $D^0X-2LO$ ), respectively. Similar results have been reported by Jesse Huso [49] and Zhang et al. [50] at the measured temperature of 82 K. Moreover, it shows weakly and broad UV peaks centered at 3.57 eV, which correspond to deep emission of the ZnMgO alloy phase. Heitsch et al. [51] have observed the same luminescence bands in MgZnO/ZnO heterostructures grown by PLD. Its peak energy position was seen to red shift from 3.57 to 3.53 eV when the MgO content was increased from  $x = 10$  to  $36$  %, respectively. This behavior is in contrast with the optical band gap increase in our Zn<sub>1-x</sub>Mg<sub>x</sub>O composites. This effect can be due to the reduction in crystalline quality and/or to the

band gap renormalization caused by many-body interactions of electron density which produces a slight downward shift on the conduction band [50]. In Fig. 8 the CL imaging analysis shows that the repartition of the emitting centers in ZnMgO is intimately connected to the film composition and surface morphology.

We observe that the luminescent centers of NBE emission at 382 nm are seemingly homogeneous for all the samples. These images show that the increase in MgO content leads to great enhancement of the UV luminescence of the ZnO bulk material. This emission is found to strongly be affected by the presence of defect-related green luminescence. Further CL studies will be carried out for better understanding the effect of Mg composition on the optical properties of Zn<sub>1-x</sub>Mg<sub>x</sub>O composites.

#### 4 Conclusion

Zn<sub>1-x</sub>Mg<sub>x</sub>O composites were synthesized by a solid-state reaction method at sintering temperature of 1200 °C. The effect of MgO doping ( $x = 0\text{--}40\%$ ) on the structural and optical properties of Zn<sub>1-x</sub>Mg<sub>x</sub>O composites was investigated. XRD analysis indicates that all the composites have prominent polycrystalline hexagonal wurtzite structure of ZnO with highly textured grains along the (002) and (101) growth directions. Above doping content  $x = 10\%$ , the formation of hexagonal ZnMgO alloy phase and the segregation of the cubic MgO phase start. Decreases in grain size and crystalline quality are observed with the increase of doping MgO content. Interestingly, there is an increase in the band gap energy from 3.287 to 3.827 eV for the composition range  $x = 0\text{--}40\%$ , respectively. This blue shift in the band gap is found to depend on the electron concentration as suggested by the Burstein–Moss effect. At room temperature, the CL spectra are dominated by a broad yellow-green emission band at 2.38 eV and ultraviolet peak at 3.24 eV corresponding to the luminescence of the hexagonal ZnO structure. Weak CL peaks also appear in the UV range (3.44–3.45 eV) as the doping MgO content is increased ( $x \geq 20\%$ ). The CL spectra recorded at 77 K showed an enhancement of the UV emissions than the green light related to oxygen defects. The CL spectra exhibit clearly the emission peaks of free exciton ( $FX_A$ ), neutral donor-bound excitons ( $D^0X$ ) and their phonon replicas. The MgO incorporation into ZnO film gives rise to new red emissions (1.68–1.8 eV) and improves the UV emission around 3.57 eV related to the ZnMgO alloy phase. CL imaging shows intensive and more homogeneous repartition of the emitting centers at 382 nm in highly doped ZnMgO composites.

**Acknowledgments** The authors gratefully acknowledge the financial support of DGRST. We are also thankful to the help rendered by Prof. Kamel Khirouni and Dr Zouhaier Ben Ayadi for absorption and diffuse reflectance measurements (LPMNE-Faculty of Sciences, Gabès, Tunisia).

#### References

1. L. Gong, J.G. Lu, Z.Z. Ye, *Sol. Energy Mater. Sol. Cells* **94**, 937 (2010)
2. S.M. Park, G.H. Gu, C.G. Park, *Phys. Status Solidi A* **208**(11), 2688–2691 (2011)
3. P.K. Kannan, R. Saraswathi, J.B.B. Rayappan, *Sens. Actuator A Phys.* **164**, 8 (2010)
4. S.T. Shishiyuan, T.S. Shishiyuan, O.I. Lu-pan, *Sens. Actuator B. Chem.* **107**(1), 379–386 (2005)
5. P. Cao, Y. Bai, D.X. Zhao, D.Z. Shen, *Mater. Sci. Semicond. Process.* **14**, 73–77 (2011)
6. Y. Uspenskii, E. Kulatov, H. Mariette, H. Nakayama, H. Ohta, *J. Magn. Magn. Mater.* **248**, 258 (2003)
7. D.K. Hwang, M.S. Oh, J.H. Lim, S.J. Park, *J. Phys. D Appl. Phys.* **40**, R387 (2007)
8. L. Li, Z. Yang, J.Y. Kong, J.L. Liu, *Appl. Phys. Lett.* **95**, 232117 (2009)
9. Y. Hu, Y. Chang, P. Fei, R.L. Snyder, Z.L. Wang, *ACS Nano* **4**, 1234 (2010)
10. Ü. Özgür, Y.I. Alivov, C. Liu, A. Teke, M.A. Reshchikov, S. Doğan, V. Avrutin, S.J. Cho, H. Morkoc, *J. Appl. Phys.* **98**, 041301–041403 (2005)
11. A.D. Acharya, Shweta Moghe, Richa Panda, S.B. Shrivastava, Mohan Gangrade, T. Shripathi, D.M. Phase, V. Ganesan, *Thin Solid Films* **525**, 49–55 (2012)
12. M.G. Nair, M. Nirmala, K. Rekha, A. Anukaliani, *Mater. Lett.* **65**, 1797–1800 (2011)
13. A. Ohtomo, M. Kawasaki, T. Koida, K. Masubuchi, H. Koinuma, Y. Sakurai, Y. Yoshida, T. Yasuda, Y. Sewaga, *Appl. Phys. Lett.* **72**, 2466 (1998)
14. Y. Ogawa, S. Fujihara, *Phys. Status Solidi A* **202**, 1825–1828 (2005)
15. A.K. Sharma, J. Narayan, J.F. Muth, C.W. Teng, C. Jin, A. Kvit, R.M. Kolbas, O.W. Manjula, G. Nair, M. Nirmala, K. Rekha, A. Anukaliani, *Mater. Lett.* **65**, 1797–1800 (2011)
16. U. Sahaym, M.G. Norton, J. Huse, J.L. Morrison, H. Che, L. Bergman, *Nanotechnology* **22**, 425706 (2011)
17. C. Jin, Growth and Characterization of ZnO and ZnO-Based Alloys Mg<sub>x</sub>Zn<sub>1-x</sub>O and Mn<sub>x</sub>Zn<sub>1-x</sub>O. Ph.D thesis. Department of Materials Science and Engineering, North Carolina State University, 2003
18. W. Yang, S.S. Hullavarad, B. Nagraj, I. Takeuchi, R.P. Sharma, T. Venkatesan, *Appl. Phys. Lett.* **82**, 3424 (2003)
19. X. Zhang, X.M. Li, T.L. Chen, C.Y. Zhang, W.D. Yu, *Appl. Phys. Lett.* **87**, 092101–092103 (2005)
20. B. Yu, X. Xu, S. Zhuang, J. Pan, J. Hu, *Mater. Lett.* **82**, 145–147 (2012)
21. S. Chakraborty, C.S. Tiwary, A.K. Kole, P. Kumbhakar, K. Chattopadhyay, *Mater. Lett.* **91**, 379–382 (2013)
22. J. Zhang, F. Pan, W. Hao, T. Wang, *Mater. Sci. Eng. B* **129**, 93–95 (2006)
23. Z.L. Liu, Z.X. Mei, R. Wang, J.M. Zhao, H.L. Liang, Y. Guo, A.Y. Kuznetsov, X.L. Du, *J. Phys. D Appl. Phys.* **43**, 285402 (2010)
24. L. Lazzarini, G. Salviati, F. Fabbri, M. Zha, D. Calestani, A. Zappettini, T. Sekiguchi, B. Dierre, *ACS Nano* **3**(10), 3158–3164 (2009)



25. S. Ilican, Y. Caglar, M. Caglar, B. Demirci, J. Optoelectron. Adv. Mater. **10**(10), 2592–2598 (2008)
26. M. Chaari, A. Matoussi, Z. Fakhfakh, Mater. Sci. Appl. **2**, 765–770 (2011)
27. P. Kumar, J.P. Singh, Y. Kumar, A. Gaur, H.K. Malik, K. Asokan, Curr. Appl. Phys. **12**, 1166–1172 (2012)
28. S.S. Hullavarad, N.V. Hullavarad, D.E. Pugel, S. Dhar, I. Takeuchi, T. Venkatesan, R.D. Vispute, J. Phys. D Appl. Phys. **40**, 4887–4895 (2007)
29. H. Endo, M. Kikuchi, M. Ashioi, Y. Kashiwaba, K. Hane, Y. Kashiwaba, Appl. Phys. Express **1**, 051201 (2008)
30. Q. Zheng, F. Huang, K. Ding, J. Huang, D. Chen, Z. Zhan, Z. Lin, Appl. Phys. Lett. **98**, 221112 (2011)
31. W. Geng, N. Li, X. Li, X. Lai, L. Wang, B. Long, J. Ning, J. Tu, S. Qiu, Mater. Res. Bull. **43**, 601–610 (2008)
32. A. Singh, A. Vij, D. Kumar, P.K. Khanna, M. Kumar, S. Gautam, K.H. Chae, Semicond. Sci. Technol. **28**, 025004 (2013)
33. W.Q. Peng, S.C. Qu, G.W. Cong, Z.G. Wang, Appl. Phys. Lett. **88**(1-3), 101902 (2006)
34. P. Kubelka, F. Munk, Z. Tech. Phys. **12** 593 (1931)
35. A.E. Morales, E.S. Mora, U. Pal, Rev. Mex. Fis. **53**(5), 18 (2007)
36. Nidhi Adhlakha, K.L. Yadav, Amit Kumar, Piyush Kumar Patel, Jyoti Rani, Meera Rawat, Physica B Condens. Matter **407** 3427–3433 (2012)
37. F.K. Shan, G.X. Liu, W.J. Lee, B.C. Shin, J. Cryst. Growth **291**, 328 (2006)
38. A. AShrafi, Y. Segawa, J. Appl. Phys. **104**, 123528 (2008)
39. X.Q. Gu, L.P. Zhu, L. Cao, Z.Z. Ye, H.P. He, P.K. Chu, Mater. Sci. Semicond. Process. **14**, 48–51 (2011)
40. F. Urbach, Phys. Rev. **92**, 1324 (1953)
41. A. Wakahara, A. Yoshida, H. Okada, H.J. Kim, H.J. Chang, K.J. Suh, Toyohashi University of Technology. <http://www.icee-con.org/papers/2005/454.pdf>
42. A. Bourguine, A. El Hichou, M. Addou, J. Ebothé, A. Kachouane, M. Troyon, Mater. Chem. Phys. **80**, 438–445 (2003)
43. A. El Hichou, A. Bourguine, J.L. Bubendorff, J. Ebothé, M. Addou, M. Troyon, Semicond. Sci. Technol. **17**, 607–613 (2002)
44. T. Minami, H. Nato, S. Takata, J. Lumin. **24**(25), 63 (1981)
45. A. Sibley, M. Nelson, Y. Chen, J. Chem. Phys. **48**, 4582 (1968)
46. M. Searlet, A.M. Glass, J. Phys. Chem. Solids **29**, 609 (1968)
47. S. Data, I.M. Boswarva, D.B. Holt, J. de Phys. **41**, C6–C522 (1980)
48. E. Feldbach, R. Jaaniso, M. Kodu, V.P. Denks, A. Kasikov, P. Liblik, A. Maaros, H. Mändar, M. Kirm, J. Mater. Sci. Mater. Electron. **20**, S321–S325 (2009)
49. Jesse Huso, John L. Morrison, Hui Che, Jency P. Sundararajan, Wei Jiang Yeh, David McIlroy, Thomas J. Williams, and Leah Bergman Journal of Nanomaterials, vol 2011, Article ID 691582
50. X.T. Zhang, Y.C. Liu, Z.Z. Zhi, J.Y. Zhang, Y.M. Lu, D.Z. Shen, W. Xu, X.W. Fan, X.G. Kong, J. Lumin. **99**, 149–154 (2002)
51. S. Heitsch, G. Benndorf, G. Zimmermann, C. Schulz, D. Spemann, H. Hochmuth, H. Schmidt, T. Nobis, M. Lorez, M. Grundmann, Appl. Phys. A **88**, 99–104 (2007)